

# Transfontanelle photoacoustic imaging: ultrasound transducer selection analysis

RAYYAN MANWAR,<sup>1,4,5</sup>  MD TARIKUL ISLAM,<sup>1,6</sup> SEYED MOHSEN  
RANJBARAN,<sup>2,4,7</sup>  AND KAMRAN AVANAKI<sup>1,3,8</sup> 

<sup>1</sup>Richard and Loan Hill Department of Bioengineering, University of Illinois at Chicago, USA

<sup>2</sup>Department of Physics, University of Isfahan, Isfahan 81746-73441, Iran

<sup>3</sup>Department of Dermatology, University of Illinois at Chicago, Chicago, Illinois 60607, USA

<sup>4</sup>These authors have contributed equally

<sup>5</sup>rmanwar@uic.edu

<sup>6</sup>mislam32@uic.edu

<sup>7</sup>ranjbaran.sm@sci.ui.ac.ir

<sup>8</sup>avanaki@uic.edu

**Abstract:** Transfontanelle ultrasound imaging (TFUI) is the conventional approach for diagnosing brain injury in neonates. Despite being the first stage imaging modality, TFUI lacks accuracy in determining the injury at an early stage due to degraded sensitivity and specificity. Therefore, a modality like photoacoustic imaging that combines the advantages of both acoustic and optical imaging can overcome the existing TFUI limitations. Even though a variety of transducers have been used in TFUI, it is essential to identify the transducer specification that is optimal for transfontanelle imaging using the photoacoustic technique. In this study, we evaluated the performance of 6 commercially available ultrasound transducer arrays to identify the optimal characteristics for transfontanelle photoacoustic imaging. We focused on commercially available linear and phased array transducer probes with center frequencies ranging from 2.5MHz to 8.5MHz which covers the entire spectrum of the transducer arrays used for brain imaging. The probes were tested on both *in vitro* and *ex vivo* brain tissue, and their performance in terms of transducer resolution, size, penetration depth, sensitivity, signal to noise ratio, signal amplification and reconstructed image quality were evaluated. The analysis of selected transducers in these areas allowed us to determine the optimal transducer for transfontanelle imaging, based on vasculature depth and blood density in tissue using *ex vivo* sheep brain. The outcome of this evaluation identified the two most suitable ultrasound transducer probes for transfontanelle photoacoustic imaging.

© 2022 Optica Publishing Group under the terms of the [Optica Open Access Publishing Agreement](#)

## 1. Introduction

In the early neonatal period, transfontanelle ultrasound imaging (TFUI) plays a significant role in detecting brain injuries [1,2]. It is particularly effective for detecting and identifying intracranial hemorrhage and ischemic insults in premature infants (<37 weeks) which occur approximately 3.5 times for every 1000 live births [3]. Complications rising from the resulting lesions lead to shunt dependence, permanent structural changes to neural tissue and other disorders such as post-hemorrhagic hydrocephalus, periventricular leukomalacia, gliosis, and neurological dysfunction [4]. The ability of TFUI to evaluate the intracranial anatomy at the neonate's bedside allows early identification of intracranial pathology, leading to reduced developmental abnormalities [5].

At birth until 9-18 months of age [6], the cranial bone formation is incomplete, and cranial bones are not fused together by sutures [7]. These gaps, known as fontanelles, are membranous tissues made of mesenchymal cells, which will mature into bone [8]. These areas, specifically the anterior fontanelle (Fig. 1(a)), provide a window for acoustic pressure waves to pass freely

through. There are several other fontanelles, however, they do not support imaging of areas of the brain most susceptible to hemorrhage. The diamond shaped anterior fontanelle (bregma) with an average size of 2~3cm, at birth, is located between the two frontal and two parietal bones of the developing neonate skull. It is at the junction of the coronal and sagittal sutures (Fig. 1(b)).

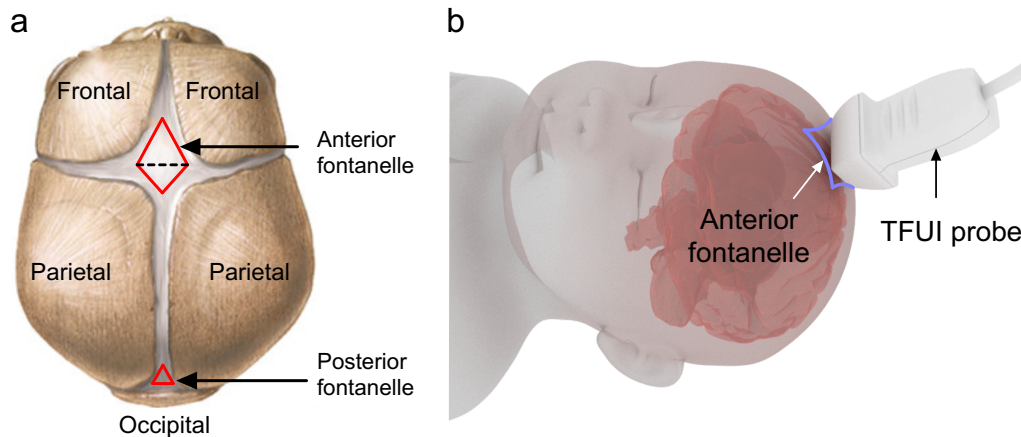


**Fig. 1.** Transfontanelle imaging (a) Fontanelle locations in a newborn baby [8], and (b) 3D rendered model demonstrating TFUI probe utilized at anterior fontanelle.

TFUI is widely used to study neonatal neuroanatomy and disease [9] as acoustic aberration is minimal due to the absence of skull bone in the fontanelle areas. TFUI has become a common protocol to use for neonatal brain imaging owing to its low cost, safety, accessibility, and non-invasive nature. TFUI has shown excellent detection capability of later stage (Grade 3-4) hemorrhagic lesions [10] [11] where sensitivity and specificity are nearly 93.3% and of 100% [12,13], respectively. However, sensitivity drastically drops to <5% [13] in detecting Grade 1-2 hemorrhage such as germinal matrix hemorrhage (GMH) and intraventricular hemorrhage (IVH). Therefore, it is crucial to opt for a cost-effective transfontanelle imaging modality that is capable of early-stage detection of hemorrhages with high sensitivity and specificity.

Photoacoustic imaging (PAI) is an emerging hybrid modality that uses a combination of optical excitation and acoustic detection, and can be utilized for visualizing vascular, functional, and molecular changes within the living tissue [14–24]. In PAI, a nanosecond pulsed laser is utilized to induce thermoelastic expansion of tissue chromophores that results in emission of acoustic waves and detected by ultrasound transducers for image formation [25–31]. PAI has already been evaluated for transcranial imaging in small animals (rats and mice) [32,33] however, neonatal brain structure and size is different from that of the rodents and has not been explored through fontanelle window yet. Since the fontanelle area has less acoustic attenuation (where, acoustic attenuation coefficient,  $\alpha = 2\text{--}3\text{dB.MHz}^{-1}$  [34]) as compared to that of skull bone ( $\alpha = 10\text{--}12\text{dB.MHz}^{-1}$  [35]), PAI is an excellent candidate [36,37] to improve the efficiency of detecting hemorrhage in neonates at an early stage.







The strength of the generated pressure signal in PAI depends on the absorption coefficient of the chromophores, the light fluence, and the characteristics of the ultrasound transducer [38]. Specifically, the photoacoustic signal containing useful information regarding the absorbing target tissue is dependant on the characteristic of the ultrasound transducer [33]. The transducer probe is desired to be structurally suitable to use at the anterior fontanelle location and the transducer probe configuration and specifications should be as such to be able to reconstruct high quality images of brain structures. Therefore, selecting an appropriate transducer probe in terms

of the center frequency, sensitivity, resolution, penetration depth, view angle, and form factor (configuration) is essential. Center frequency of the transducer is selected based on the desired resolution and penetration depth. Utilizing low frequency probes in the range of 1-3MHz [39] allows for better penetration and consequently can acquire signal from deeper brain structures, up to 5~6cm [40]. The drawback, of low transducer frequency is degraded image resolution. To improve the image resolution, we can utilize higher frequency transducers (4-10MHz). In the fontanelle area due to the absence of skull bone, we anticipate less attenuation of acoustic pressure waves, thus possibly allowing the use of higher center frequency transducers. We expect this frequency range to provide a penetration of the neonatal brain of up to 3.5cm at high resolution [40,41].

High acoustic transducer sensitivity can be achieved by increasing the active sensing surface area, number of the elements, coupling efficiency, and bandwidth [42]. Coupling efficiency and bandwidth is directly linked to transducer material properties and fabrication process as explained in [38]. Among different aperture and sensing configurations of the transducer, linear and phased arrays are preferable for transfontanelle imaging over complex multiple single element and ring arrays due to their complexity in placement on the fontanelle area and data acquisition [43]. However, the preferred linear or phased array transducer sensing surface and number of elements is limited by the acoustic window of the anterior fontanelle which also constricts the view angle. Linear arrays have comparatively large footprint area with high sensitivity and number of elements. This is the simplest form of array configuration and are available in a wide range of center frequencies [44]. Phased array transducers are also popular due to their smaller footprint and wider view angle as compared to linear array specifically where the acoustic window is limited. However, these are commercially available in the limited frequency range (2.5-8.5MHz) [45]. Despite the different characteristics of linear and phased arrays, evaluation of these transducers has not been performed in transfontanelle imaging using photoacoustic technology. Vogt et al. [46] has compared the performance of four different transducers on a breast tissue mimicking phantom and focused on developing standard test methods to characterize PAI systems. However, this study was not further performed on actual tissue and the objective was not to determine the most suitable probe for brain imaging where several restrictions must be considered (e.g., increased optical and acoustic attenuation, limited PA probe placement area, limited imaging window).

Here, we have categorically evaluated the performance of several transducer arrays as shown in Table 1 (linear arrays: L7-4, L12-5 38 mm and 50 mm, and CL 10-5, and phased arrays: P4-2 and P6-3) to determine the most suitable transducer for transfontanelle photoacoustic imaging. These specific transducer arrays were chosen based on their respective center frequencies that cover the whole spectrum of ultrasound transducers used for brain imaging. In the next section, we have provided the transducer specification along with phantom preparation techniques. The initial experiments in water and optically attenuated medium were performed to provide default performance and impact of optical attenuation on transducer performance. Later, we utilized a brain tissue mimicking phantom to represent the acoustic and optical characteristics of brain tissue. Transducer evaluation is based on the resolution, penetration depth, sensitivity, signal to noise ratio (SNR), contrast to noise ratio (CNR) and amplifier compatibility. Analysis of selected transducers in these areas allowed us to determine the optimal transducer for transfontanelle imaging, based on vasculature depth and blood density in tissue using *ex vivo* sheep brain.

Table 1. Specification of the transducer arrays

Configuration	Linear				Phase	
Model						
	CL10-5	L7-4	L12-5 38mm	L12-5 50mm	P4-2	P6-3
Manufacturer	ATL Philips	Philips	ATL Philips	ATL Philips	Philips	ATL Philips
Center Frequency (MHz)	6.25	5.2	7.8	8.5	2.5	4.46
Bandwidth (MHz)	80%	57.7	89.7	82.4	80	67.3
No. of elements	128	128	192	256	64	128
Pitch (mm)	0.2	0.29	0.20	0.19	0.32	0.22
Element size (mm)	0.15	0.25	0.17	0.17	0.3	0.19
Lateral Aperture size (cm)	2.56	3.71	3.84	4.86	2.04	2.84

## 2. Material and methods

### 2.1. Experimental instrumentation

To evaluate the performance of transducer arrays for transfontanelle photoacoustic imaging, we used a Q-switched Nd:YAG Opotek Phocus HE MOBILE laser (OPOTEK, LLC, USA) with a pulse width of 5-7 ns and repetition rate of 10 Hz. The target was illuminated by the laser through a bifurcated fiber bundle (consists of 414 silica fibers, 200 $\mu$ m core diameter, and 130 cm length) with a numerical aperture of 0.22, manufactured by Fiberoptics Technology Inc. (Pomfret, CT, USA). On the laser side, there was a 5.5 mm diameter stainless-steel ferrule with an active aperture of 5.0 mm, and on the imaging target side there were two 22 mm  $\times$  0.80 mm rectangular bifurcated metal plates with an active aperture of 17 mm  $\times$  0.64mm, secured to the fixture by a 3D-printed holder at 10 angle from the transducer probe. The position and angle of the fiber bundle active aperture to the probe viewing plane was specifically optimized to illuminate the test area homogenously at a 1 cm distance from the probe tip. The maximum input energy to the fiber bundle was measured 135mJ at 750nm and the measured fluence at the target was 30mJ/cm<sup>2</sup>. The schematic of the experimental setup is shown in Fig. 2(a). For performance evaluation and comparison, we have chosen 6 transducer arrays (Table 1) with two different configurations (i.e., linear and phase). The center frequency of the transducer probes is in the range of 2.1-8.5 MHz that encompasses the conventional transducer frequency used for brain imaging [47,48]. The transducer probes were kept at a distance of  $\sim$ 1.5cm from the imaging target. The specifications of the transducer arrays are provided in Table 1.

For data acquisition, we utilized a Vantage 128 (Verasonics Inc., Kirkland, WA, USA) with a sampling rate of 62.5MHz. The receive frequency response range for Vantage 128 is 0.5MHz to 50MHz with a programmable anti-aliasing filter cut-off at 5, 10, 15, 20, 30, and 35.5MHz. To synchronize the data acquisition with the laser firing, we have followed the connection scheme as presented in [49]. We have utilized the Verasonics proprietary algorithm to reconstruct B-mode images. The gain settings have been kept consistent for all the data processing.



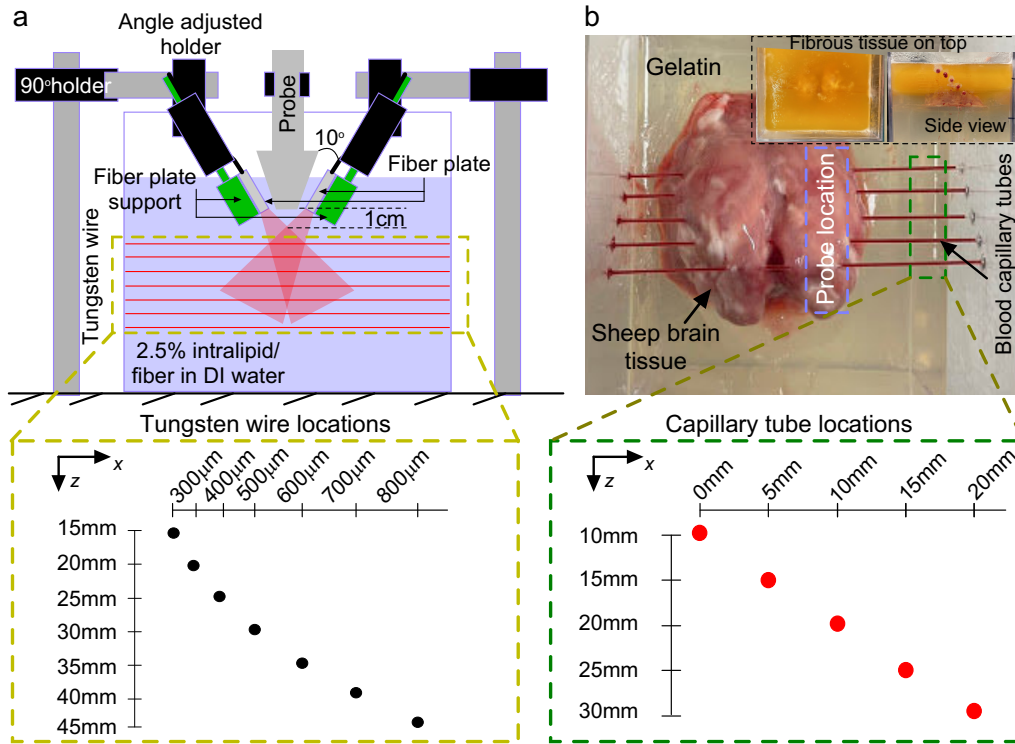


**Fig. 2.** Experimental setup for transfontanelle photoacoustic imaging *in-vitro* and *ex-vivo* (a) schematic of the experimental setup- a cross-sectional view of the target wire phantom location is expanded in light green box, and (b) top view of the *ex-vivo* sheep brain tissue with 4 glass capillary tube (1mm diameter) filled with sheep blood. The capillary tube locations are shown in the cross-sectional view in dark green box. The distance in the axial direction (z axis) is between the transducer surface and the target location. The top capillary tube was located at 3mm from the brain tissue surface.

## 2.2. Phantom preparation

To establish the baseline quality of the images reconstructed from the proprietary algorithm by Verasonics, the resolution phantom container was filled with distilled (DI) water and the PA data was acquired. For accurate evaluation and further comparison among the transducers, there were no other post-processing methods applied on the reconstructed images.

Biological tissue (e.g., brain tissue) is an optically turbid media. Therefore, to evaluate transducer suitability in that environment, we used a 2.5% intralipid medium to represent the optical properties of brain tissue [44] and assessed the impact on the performance of each transducer. Similarly, an acoustical attenuating medium made of 5% water-soluble fiber (Psyllium husk) in DI water was added to the intralipid medium to represent both optical and acoustic properties of brain tissue [50]. Other alternatives (e.g., Silica particles, glass microspheres) can also be as acoustic scatterer [51–53].

For the *ex-vivo* study, decapitated sheep heads were processed to extract the whole brain tissue and placed inside an open-top transparent plastic cube. To keep the brain tissue in place, the container was filled with 8% gelatin (Fig. 2(c)), leaving a  $2 \times 0.5 \text{ cm}^2$  area of brain tissue exposed (blue dashed box), and left to cure. Once, the sheep brain was fixed in gelatin, we poured a 2.5% fiber solution mixed in 8% gelatin to cover the exposed tissue area, representing the fibrous

fontanelle area of neonates. To couple the transducer arrays, rest of the container was filled with DI water. Small holes of 1.5mm diameter were created on the wall of the box and 1mm inner diameter glass capillary tubes were inserted at different depth (10, 15, 20, 25, and 30mm) and filled with sheep blood to mimic vessel like structures. The capillary tubes were 5mm apart in lateral direction.

### 2.3. Data processing

Lateral, axial, and elevation resolutions were measured from the reconstructed images based on the full width half maximum (FWHM) of line spread function (LSF) at different depths ranging from 15–45mm (average neonatal brain height is 30mm). Axial and lateral LSFs were acquired by extracting horizontal and vertical line profiles across the reconstructed cross-sectional image of the target. Elevation LSF was generated by mechanically scanning the transducer using a 3D motorized stage along the short axis of a wire target [46]. The lateral axis of the transducer array was aligned along the tungsten wire. For mechanical scanning, the transducer and the optical fiber bundle both were attached to the 3D stage. Therefore, the relative position between the transducer and the fiber bundle was always constant and the signal would only disappear when the imaging target was completely out of imaging plane. Scanning step size was 10 $\mu$ m. Scanning continued until the target object was no longer visualized on the reconstructed image. The SNR and CNR were calculated based on the peak-to-peak A-scan data and noise floor of respective probes. To determine the noise floor, we have considered the peak-peak noise amplitude from a sample length of 200, 100 samples prior to the sample number where the N-shaped PA signal starts to rise and another 100 samples after the N-shaped signal settled down, with a buffer of 50 samples. This buffer of 50 samples was considered based on the decrement in axial resolution. For each experimental phase, a total of 20 datasets for each probe was averaged to extract the SNR, CNR, and attenuation values. The attenuation was extracted for *in vitro* and *ex vivo* studies based on the difference between the PA signal amplitude from target object when immersed in water medium and other media. To calculate the signal attenuation due to introducing the scattering medium in comparison to ideal scenario, a compensation technique was utilized by multiplying the gain difference to the A-scan signal acquired in the DI water.

To evaluate the sensitivity profile, we diluted blood samples with 1  $\times$  phosphate buffered saline (PBS). Based on an iterative process (each transducer was used to image sheep blood sample with a gradually decreasing concentration starting from 100% down to 10%) and we found that 20% blood in PBS as imaging target inside brain tissue would be the minimum concentration that can be visualized in the reconstructed images at a maximum of 30mm depth. Based on the average pixel intensity at different depths (15–30mm) within brain tissue, the sensitivity profile of the each of the probes was evaluated. A Legion 128 Amp (Photosound Technologies, TX, USA) amplifier with analog bandwidth 40kHz–35MHz was used to evaluate the impact of an amplifier on both PA signal and background noise signal. For this experiment, we used a 3mm inner diameter tygon tube (1mm outer diameter) filled with 100% sheep blood. The optical absorption by the tubing was compensated based on the PA signal generated from the tube walls when filled with 1  $\times$  PBS only. We evaluated the amplifier impact on the acquired data by each transducer based on the true PA signal intensity enhancement as compared to the increment in the noise level after amplification.

## 3. Results and discussion

To establish the baseline performance, the wire phantoms were immersed in DI water. Each probe was placed normal to the wire and at 90° to image the cross-section. For resolution analysis, the B-mode images (Fig. 3(a)) of the wire phantoms were captured by each of the transducer probes at minimal gain ( $\sim$ 0.5 dB) and high rejection rate ( $\sim$ 90%) to avoid any saturation in the image. This gain value has been compensated for in the results shown in the next steps. At each

depth, straight lines (vertically and horizontally) were drawn across the PA images of the target wire to generate the axial and lateral LSFs and the resolution was extracted from the FWHM of the LSF Gaussian profile. Elevation LSF was generated from the lateral dimension of the image stack volume and corresponding resolution was calculated from the FWHM of the LSF. All the transducers provided poor elevation resolution relative to axial and lateral resolution. The extracted resolutions are shown in Fig. 3(b). Since, L12-5 probes and

CL10-5 have a center frequency in the range of 6.25MHz and 8.5MHz, both resolutions have insignificant differences within the range of 0.39-0.48mm and 0.5-0.6mm, respectively up to a depth of 35mm. Among all the transducers P4-2 provides the lowest average resolution (0.51mm, 0.63mm, 3.91mm) as a function of depth followed by P6-3 and L7-4. However, P4-2, P6-3 and L7-4 probes are capable of imaging targets in the phantoms located up to 45mm (7 wires). The high frequency probes (L12-5 series and CL10-5) provide limited penetration depth and can only image up to 35 mm, therefore, the rest of the evaluation for *in-vitro* study was conducted using only the top five wires in the phantom. The calculated SNR and CNR are provided in Fig. 3(c). Even though CL10-5 has the highest SNR of 40dB at 15mm depth, the SNR decreases to 16.2dB at 35mm depth. A similar trend can also be seen in the L12 series probes. In addition, CL10-5 and both L12-5s show degraded performance in terms of the CNR as a function of depth. Among the transducer probes, L7 and P6-3 provides the highest SNR (22.7dB) and CNR (13) respectively at 35mm depth.

Next, we evaluated the performance of the transducer probes when the target wire phantoms were immersed in optical scattering medium. The reconstructed B-mode images are shown in Fig. 4(a). In order to calculate the resolution from FWHM, we kept the adjustable gain to a minimum to avoid any saturation in the line profile. However, once we added the optically attenuating medium, to visualize in the reconstructed image, we increased the gain to the maximum. Therefore, while calculating signal amplitude attenuating, this gain difference was compensated based on the gain value defined in the MATLAB script. Due to the optical scattering effect, as the depth increased, we can only visualize four targets using CL10-5 (fifth target can be distinguishable from the A-scan data), whereas with other linear and phased arrays we can visualize all five targets. However, due to higher center frequency of the L12 series as compared to L7-4 and phased arrays, the PA intensity has greatly been impacted. As compared to the base line experiment in DI water only, here the SNR and CNR have been reduced by 10 times. This scenario is evident in the SNR and CNR evaluation shown in Fig. 4(b). Since, L12-5 50mm has a larger aperture with 256 elements, therefore, the SNR and CNR are higher than L12-5 38mm (element no. 192) and CL10-5 (element no. 128). P6-3 was the least impacted and provides the highest SNR and CNR due to low frequency, smaller footprint with higher number of the elements as compared to L7 and P4-2 respectively. The geometric focus of the probes is in the range of 22-27mm and hence, the overall attenuation was minimal in between that depth range (Fig. 4(c)). The signal acquired by CL10-5 was attenuated the most (14.3 dB at a depth of 15mm and 12.15dB at 35mm). L7-4 and P6-3 has the lowest average attenuation of 4.8dB and 3.76dB, respectively.

Once, the impact of the optical scattering medium was evaluated, we introduced acoustic absorption and scattering to the phantom; the reconstructed images are shown in Fig. 5(a). The grainy artifact in the image is due to the presence of the fiber made from psyllium husk. The mixture of intralipid and fiber also acted as optical absorbers similar to white and gray matter, therefore more background noise is visualized in B-mode images and maximum SNR and CNR level drop by 5-6 dB, respectively (Fig. 5(b)). Qualitatively, the L12-5 38mm acquired maximum background noise hence the SNR is in the range of 7.83 - 12.67dB. The performance of CL10-5 and P4-2 is comparable for both SNR and CNR. CL10-5 is impacted by the acoustic attenuation due to high frequency with small aperture therefore provided a lower SNR (11.25-19.89dB), whereas P4-2 is impacted by the background noise due to the low center frequency and resolution,

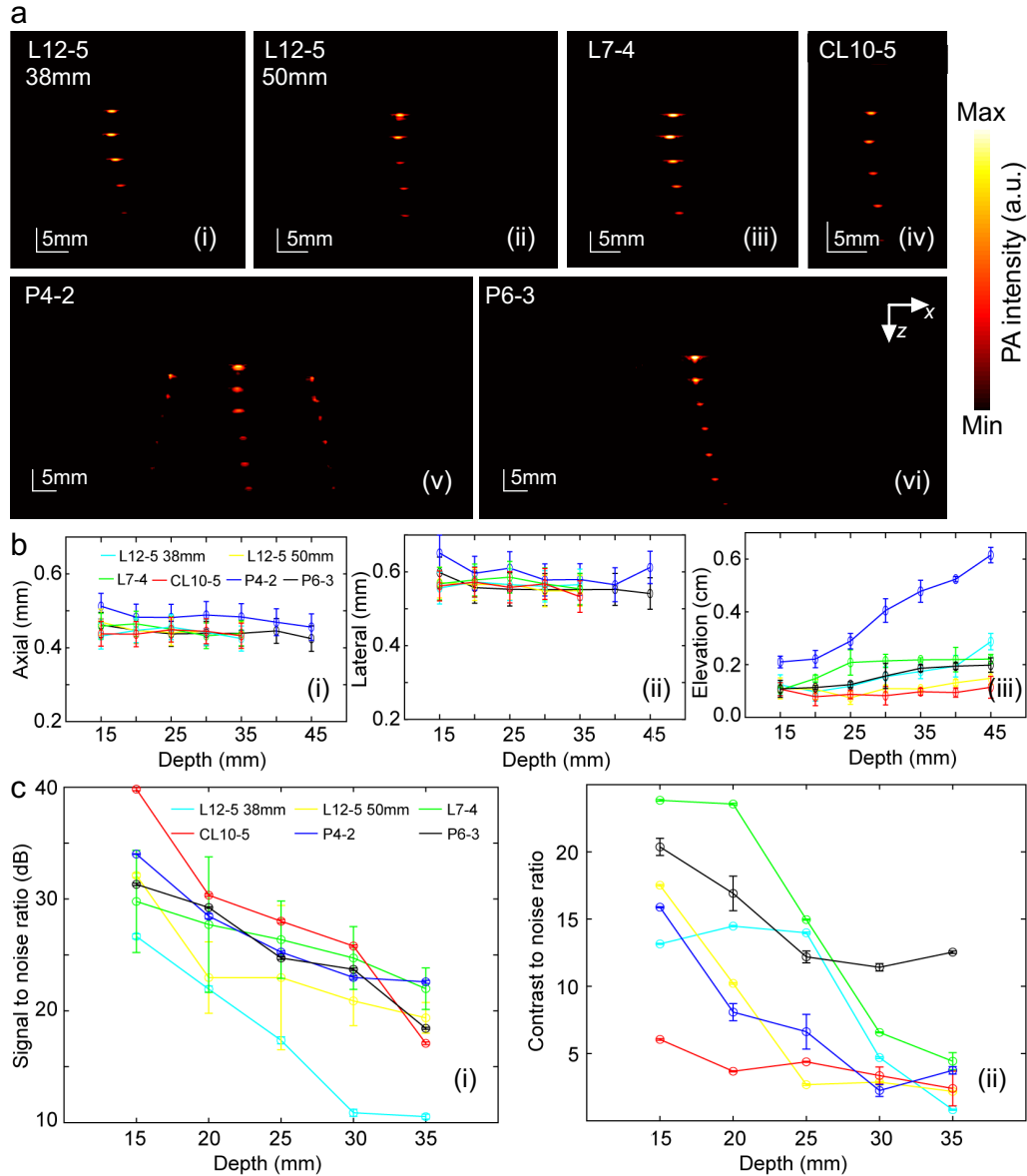


**Fig. 3.** Resolution study and comparative analysis of the baseline performance by probes in ideal scenario (a) Reconstructed B-mode images of *in vitro* wire phantom in DI water medium, (i) L12-38mm, (ii) L12-50mm, (iii) L7-4, (iv) CL10-5, (v) P4-2, (vi) P6-3, (b) resolution as a function of depth from 15 - 45mm (i) axial, and (ii) lateral, (iii) elevation (c) performance evaluation based on (i) SNR, and (ii) CNR. Standard deviation is shown using error bars.

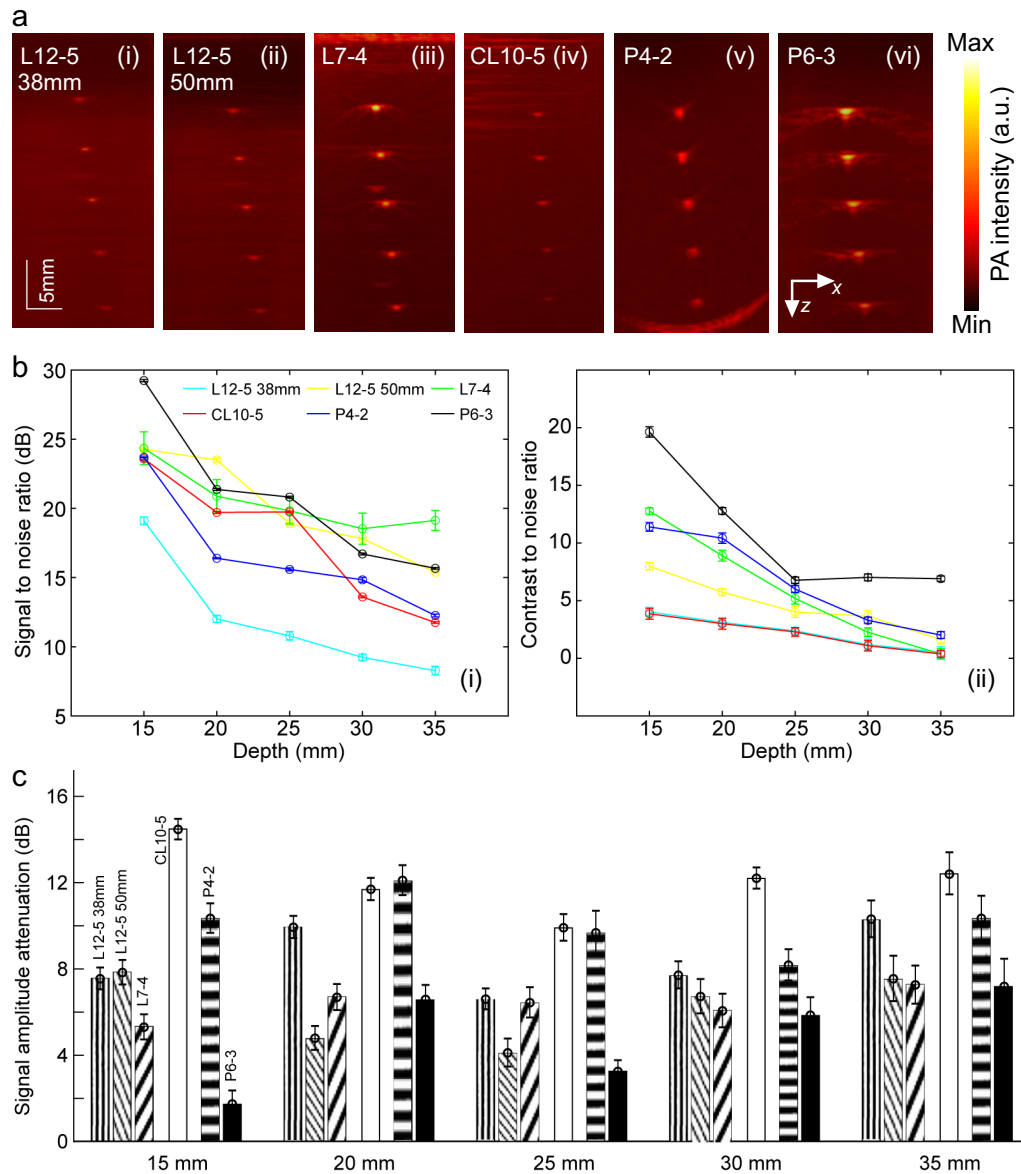


**Fig. 4.** Comparative analysis of the probe performance in optically attenuating medium (a) Reconstructed B-mode images of *in vitro* wire phantom in 2.5% intralipid in DI water, (i) L12-38mm, (ii) L12-50mm, (iii) L7-4, (iv) CL10-5, (v) P4-2, (vi) P6-3, (b) performance evaluation based on (i) SNR, and (ii) CNR. Standard deviation is shown using error bars, and (c) PA signal amplitude attenuation due to optical scattering medium at different depths (15-35mm). The signal amplitude acquired when only DI water was used as medium has been considered as an ideal signal.



hence provided the minimum CNR (0.2-1.2). L12-5 50mm provided better distinction between the signal and the noise however, the performance is degraded in terms of CNR. L7-4 and P6-3 both provided stable performances as a function of depth where average SNR of the P6-3 was 3dB higher and CNR was only 0.3 times higher as compared to L7-4. The overall attenuation was reduced by an average of ~9dB among the transducer arrays. The attenuation for each of the probes in intralipid and fiber combined medium was calculated by comparing to the baseline signal amplitude and presented in the Fig. 5(c). The highest attenuation was observed from CL10-5 followed by L12-5 38mm and P4-2. L7-4 and P6-3 had the least average attenuation of 7.45dB and 6.29dB.

After establishing the performance trend *in vitro*, the transducer probes were tested with *ex vivo* sheep brain tissue. Due to the overall height (~35mm) of the sheep brain tissue, we have used five glass capillary tubes filled with sheep blood at different depths (10-30mm) with 5mm gap in both axial and lateral direction, as shown in Fig. 2(c). The capillary tube locations in the image are shown using white arrows. The majority of the optical energy was initially absorbed by fontanelle tissue mimicking layer and the brain tissue surface. The diffused energy inside the brain tissue is mostly absorbed by the blood within the glass capillary tube. However, the acoustic pressure wave propagating back to the probe partially reflects back from the blood-capillary tube wall and capillary tube wall-brain tissue interface. That is probably the reason for the reverberation (shadow effect) which is present after the tube locations axially in the *ex-vivo* reconstructed images (Fig. 6(a)). CL10-5 and P4-2 were not able to reconstruct the B-mode image of the 5<sup>th</sup> capillary from the top (Fig. 6(a) iv and v). For these particular case, the extracted performance parameters were evaluated from the A-scan data.

The limitation of L12 series probes can be visualized in the reconstructed images where the target wire phantom is distorted as the depth increases. L12 series probes contain more than 128 elements and therefore, at least two separate acquisition apertures (96 and 128 elements in each aperture of L12-5 38mm and 50mm respectively) are required in Vantage 128 system. The source of this distortion could be the superposition of the two acquisition apertures from two different laser pulses. The Vantage operation flow diagram is shown in Fig. 7. Due to the initial optical energy loss at the tissue surface, the maximum SNR was decreased for L12-50mm among all the probes by 16dB at 10mm depth and 11.2 dB at 30mm depth (Fig. 6(b) (i)). As the depth increased, the SNR from high frequency probes (L12 series and CL10-5) was decreased at a higher rate (maximum  $0.27\text{dBmm}^{-1}$  for L12-38mm) as compared to the other three probes (average SNR decay rate:  $0.14\text{dB/mm}$ ). Overall performance in terms of CNR was comparable to the *in vitro* results (Fig. 5(b)(ii) and Fig. 6(b)(ii)). CNR of L12-5 50mm, L7-4, and P6-3 at the shallow depth of 10mm were 9.82, 9.78, and 13.45, respectively, and dropped to 1.8, 3.4, and 3.9, respectively where the 5<sup>th</sup> capillary was located at 30mm depth. CL10-5 and P4-2 provided the least CNR at all the depths. (0.93 and 1.8 respectively at 30mm depth). Signal amplitude attenuation is presented in Fig. 6(c) where L12-5 38mm had the highest attenuation among all the transducer probes with a maximum of 32.3dB occurring at 30mm depth followed by P4-2 (27.5dB) and CL10-5 (26.8dB). The attenuation for L12-5 50mm and L7-4 were comparatively less compared to other transducers (24.5dB and 22.3dB respectively at 30 mm depth). The performance of P6-3 was impacted the least due to the brain tissue medium in terms of signal amplitude attenuation of 12.4, 14.7, 15.1, 17.8, and 20.3dB at 10-30mm depth with a step size of 5mm.

We have characterized the transducer sensitivity profile to low concentration blood samples at different depths (15-30mm) as shown in Fig. 8(a). Among all the transducer probes L12-5 50mm, L7-4, and P6-3 provided greatest sensitivity at depths up to 25 mm (equivalent to lateral ventricle location in the brain tissue [54]). The sensitivity was normalized to find out which transducer probe provided the least decay in sensitivity as a function of depth. Among the top four probes, CL10-5 showed the least average sensitivity decay (28.4%), followed by L7-4 with a

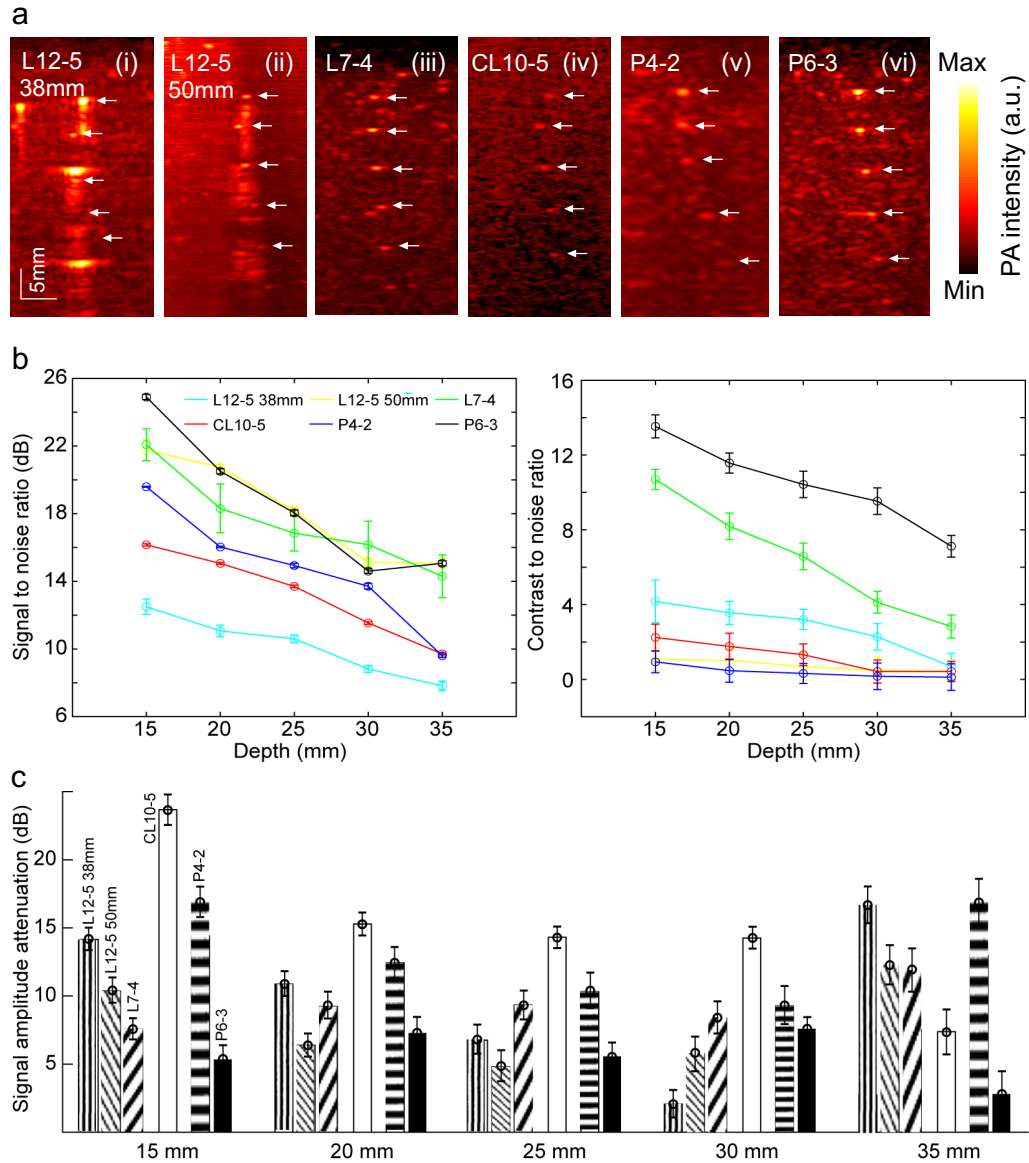


**Fig. 5.** Comparative analysis of the probe performance in both optical and acoustic attenuating medium (a) Reconstructed B-mode images of *in vitro* wire phantom immersed in tissue mimicking medium (2.5% intralipid and 5% fiber), (i) L12-38mm, (ii) L12-50mm, (iii) L7-4, (iv) CL10-5, (v) P4-2, (vi) P6-3, (b) performance evaluation based on (i) SNR, and (ii) CNR. Standard deviation is shown using error bars, and (c) PA signal amplitude attenuation due to optical scattering medium at different depths (15-35mm). The signal amplitude acquired when only DI water was used as medium has been considered as an ideal signal. Target locations are shown with white arrows.

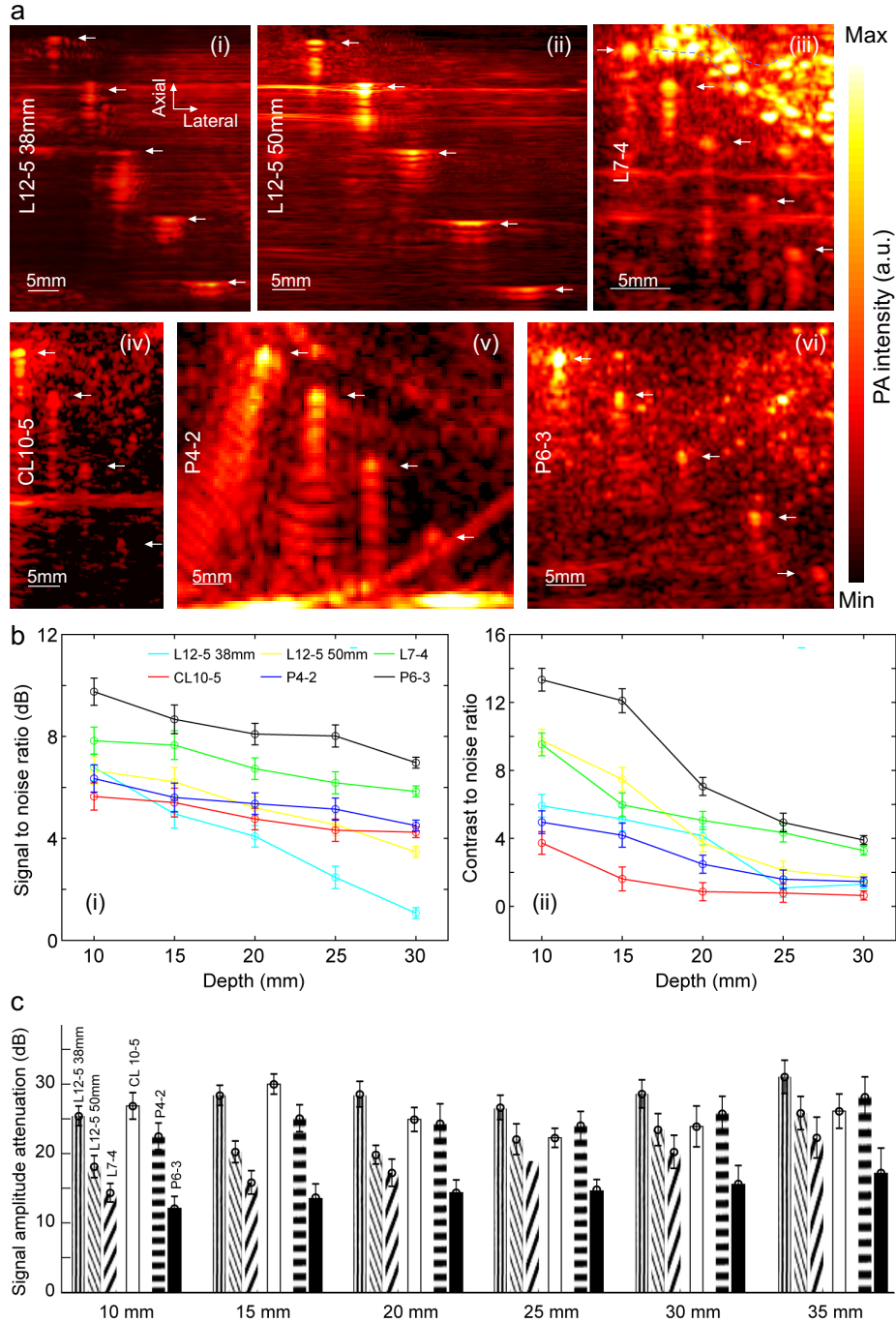


**Fig. 6.** *Ex-vivo* comparative analysis of the probe performance in excised brain tissue medium (a) Reconstructed B-mode images of *ex vivo* sheep brain tissue immersed in 8% gelatin and fibrous tissue mimicking phantom, (i) L12-38mm, (ii) L12-50mm, (iii) L7-4, (iv) CL10-5, (v) P4-2, (vi) P6-3, (b) performance evaluation based on (i) SNR, and (ii) CNR. Standard deviation is shown using error bars, and (c) PA signal amplitude attenuation due to optical scattering medium at different depths (10-30mm). The signal amplitude acquired when only DI water was used as medium has been considered to be the ideal signal. The blue dashed line shows the brain tissue and fibrous fontanelle interface. Target locations are shown with white arrows.

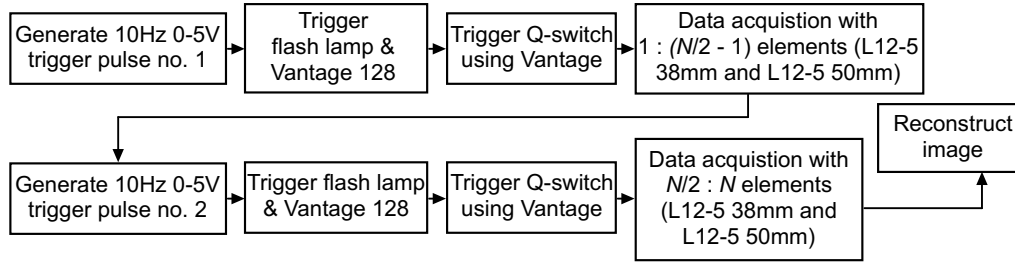


**Fig. 7.** Vantage 128 operation flow diagram for L12 series probes in photoacoustic imaging.

decay of 48.6%, L12-5 50mm (49.8%), and P6-3 (58.5%). However, due to high attenuation of the PA signal acquired by the CL10-5, the maximum sensitivity at shallow depth (15mm) was equivalent to the sensitivity of other three probes observed at a depth of 25-30mm.

One of the main challenges of brain imaging using the photoacoustic technique is to induce sufficient acoustic pressure wave from limited optical energy deposition and hence, amplifiers are often utilized to enhance the signal strength. Here, we have tested the impact of a Legion 128 Amp (Photosound, Technologies, TX, USA) on the acquired data by the probes and compared the amplitude of the true PA signal and the noise floor as shown in Fig. 8(b). Signal amplification of L7-4 and P6-3 appear best with Legion amplifier; the PA signal was amplified by 65.7% and 47.1% more than the noise levels respectively. The amplifier was more susceptible to the noise band of L12-5 series probes, therefore, the noise floor was amplified.

Structurally, the main challenges in transfontanelle photoacoustic imaging are the small fontanelle window size and rapid formation of skull bone near the opening; i.e., on the first day of life, the normal fontanel ranges from 0.6–3.6 cm, with a mean of 2.1 cm [55]. Furthermore, unlike TFUI, for efficient transfontanelle photoacoustic imaging, the optical energy must be delivered through the fontanelle window [56]. Therefore, a smaller footprint of the transducer array is desired. The footprint area (lateral  $\times$  elevation) of the probes used in this article are L12-38mm:  $53.4 \times 21.1 \text{ mm}^2$ , L12-50mm:  $66.6 \times 22.9 \text{ mm}^2$ , L7-4:  $52.1 \times 20.9 \text{ mm}^2$ , CL10-5:  $34.3 \times 11.8 \text{ mm}^2$ , P4-2:  $27.2 \times 18.6 \text{ mm}^2$ , P6-3:  $34.2 \times 23.6 \text{ mm}^2$ . The lateral dimension of L12 series and L7-4 probes cannot be fully accommodated within the maximum fontanelle window. 32% (~69 elements) of L12-38mm and 46% (~117 elements) of L12-50mm, and 31% (~40 elements) of L7-4 will be outside the fontanelle window. The elements located outside the fontanelle will be facing the skull bone and the acquired data by those specific elements will negatively affect the reconstructed image due to skull aberration [38]. Loss of active elements on the edges of the array lead to reduced viewing angle and acquired data amplitude. Therefore, the reconstructed images tend to be highly distorted and rapid increase of attenuation as the depth increases is observed.

Here, one of the main objectives was to test and observe the transducer behavior when exposed to optically and acoustically turbid medium (Fig. 4 and 5) as compared to ideal scenario (DI water) where optical and acoustic scattering media are absent (Fig. 3). Despite the fact that specific transducer arrays (e.g. CL10-5, P4-2, L12-5) exhibit better performance as compared to other arrays in an ideal scenario, they are more sensitive to noise when operated in a tissue mimicking phantom. The changes in the transducer behavior were evident when the optical and acoustic scattering medium have been introduced. Based on the performance evaluation of the transducer probes in both *in vitro* and *ex vivo*, we have presented a qualitative comparison in Table 2. CL10-5 and L12-5 38mm are more susceptible to noise and since the center frequency is comparatively higher than L7-4 and P series probes, the impact of the optical and acoustic

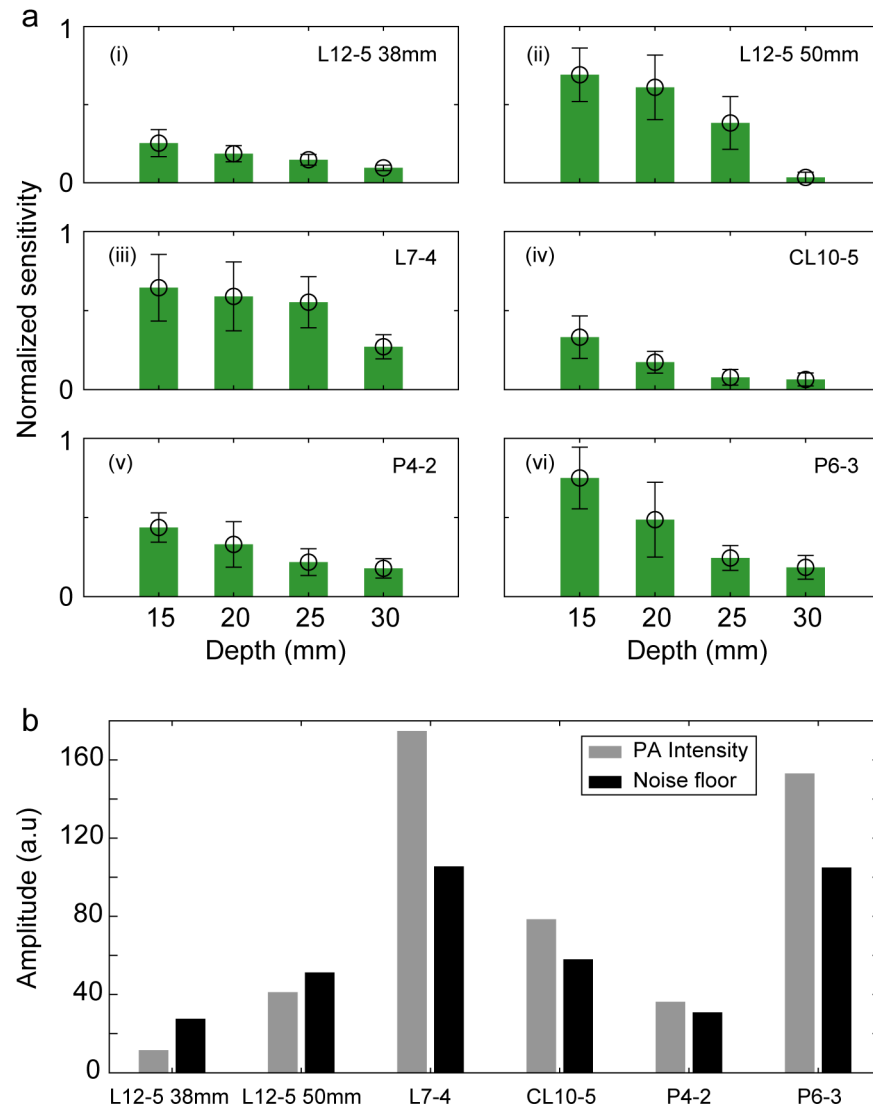


**Fig. 8.** Transducer sensitivity profile and impact of amplifier when imaging low concentration *ex-vivo* blood samples, (a) Normalized sensitivity of (i) L12-5 38mm, (ii) L12-5 50mm, (iii) L7-4, (iv) CL10-5, (v) P4-2, and (vi) P6-3 at different depths ranging from 15-30mm inside *ex-vivo* brain tissue, (b) True photoacoustic signal amplitude and noise amplitude after amplification.



attenuation is abrupt specifically at higher depths. Despite the high center frequency, CL10-5 suffers from limited field of view problem due to smaller footprint area. L12-5 50mm showcased high SNR and CNR with lower attenuation as compared to its counterpart (38mm) due to larger aperture size and a greater number of elements. However, the footprint of the probe is quite large, and half of the elements will be outside the fontanelle area and blocked skull bone. P4-2 is a suitable candidate in terms of footprint area and imaging deeper structures within the brain tissue, however, the image quality (SNR and CNR) is degraded due to high background noise and inherent low center frequency. L7-4 and P6-3 have a center frequency of 5.2 and 4.5MHz with a bandwidth of 57% and 66% which enables to achieve relatively high resolution as compared to lower frequency narrow band probes (i.e. P4-2) and better penetration as compared to higher frequency probes (i.e., CL10-5). Moreover, both the probes consist of 128 elements and do not have severe distortion effect that was visualized in the reconstructed images by L12 series probes in which two aperture acquisitions were used. In addition, being a phased array P6-3 is capable of providing a wider field of view with a smaller footprint which is desirable for the transfontanelle imaging.

**Table 2. Comparative performance analysis of the transducer arrays for transfontanelle photoacoustic imaging**

Categories	CL10-5	L7-4	L12-5 38mm	L12-5 50 mm	P4-2	P6-3
Size (mm <sup>2</sup> )	2.56 × 0.15	3.71 × 0.25	3.84 × 0.17	4.86 × 0.17	2.84 × 3.0	2.04 × 0.19
Resolution (mm)	0.42	0.45	0.43	0.43	0.49	0.46
Penetration depth (cm)	3.5	4	3.5	4	4.5	4.5
SNR (dB)	4.8-5.7	6.1-7.9	1.2-6.7	3.9-6.7	5.2-6.2	7.7-9.8
CNR	0.5-3.9	2.1-9.6	1.8-5.9	3.6-9.8	1.7-4.8	3.9-13.7
Sensitivity (a.u.)	0.16	0.51	0.17	0.43	0.29	0.42
Lateral field of view (cm)	2.5	3.7	3.8	5	6	7

#### 4. Conclusion

Transfontanelle ultrasound imaging is the first stage of diagnostic protocol to primarily determine the location and size of hemorrhagic lesions right after a baby is born with complications. Due to the limited ability of the ultrasound imaging modality to extract structural and functional information it is unable to identify early-stage hemorrhages. However, photoacoustic imaging is capable of identifying early-stage hemorrhages due to a high sensitivity of absorption-based optical contrast and a deep acoustic penetration. To efficiently use the photoacoustic technique for transfontanelle imaging, we need to identify an appropriate transducer probe. Here, we have evaluated six different probes (L12-5 38mm, L12-5 50mm, L7-4, CL10-5, P4-2, and P6-3) based on their resolution, SNR, CNR, and attenuation. Initially, we have compared their performance in DI water and established the base line performance. Further, we have tested the probes when impacted by only optically scattering medium, followed by tissue mimicking phantom by introducing acoustic attenuating medium. We have tested the probes by imaging blood filled capillary tubes in *ex-vivo* brain tissue. CL10-5 and L12-5 38mm has a high resolution however, they are prone to capture noise and their attenuation is very high, thus limited imaging depth. P4-2 is not capable of providing sufficient resolution and is less sensitive due to its narrow bandwidth, therefore its SNR and CNR both are low. L12-5 50mm performed well in optical scattering medium, however, the performance was degraded when exposed to acoustically attenuating medium. We have also analyzed the transducer array sensitivity profile to the low concentration blood at various depths and compatibility with an amplifier. Finally, we have discussed the

structural constraints of the fontanelle on neonatal head and the footprint of the transducer arrays for optimum utilization of the photoacoustic probe on the anterior fontanelle window. Based on our comparisons, we found that L7-4 and P6-3 are two suitable candidates, where P6-3 possess additional structural (small aperture) and technological (phased – wider view angle) advantage over L7-4. Considering the promising capabilities of photoacoustic brain imaging, this work is the first step towards developing a PAI system for transfontanelle imaging.

**Funding.** National Institutes of Health (R01EB027769-01, R01EB028661-01, R21 DA052657-01).

**Disclosures.** The authors have no conflicts of interest to report.

**Data availability.** Data underlying the results presented in this paper are not publicly available at this time but may be obtained from the authors upon reasonable request.

## References

1. H. L. Cohen and N. Blitman, "Neurosonography of the infant: diagnosis of abnormalities," in *Ultrasonography of the Prenatal and Neonatal Brain* 259–285 (1996).
2. D. J. Rubens, "Diagnostic ultrasound: a logical approach," *Radiology* **208**(3), 640 (1998).
3. M. Heron, P. D. Sutton, J. Xu, S. J. Ventura, D. M. Strobino, and B. Guyer, "Annual summary of vital statistics: 2007," *Pediatrics* **125**(1), 4–15 (2010).
4. T. Lekic, D. Klebe, R. Poblete, R. Krafft, B. Rolland, J. Tang, and H. Zhang, "Neonatal brain hemorrhage (NBH) of prematurity: translational mechanisms of the vascular-neural network," *Curr. Med. Chem.* **22**(10), 1214–1238 (2015).
5. D. R. Patel, M. Neelakantan, K. Pandher, and J. Merrick, "Cerebral palsy in children: a clinical overview," *Trans. Pediatr.* **9**(S1), S125–S135 (2020).
6. B. J. Lipsett and K. Steanson, "Anatomy, head and neck, fontanelles," In *StatPearls [Internet]*, StatPearls Publishing: 2019.
7. K. Nakashima and B. de Crombrughe, "Transcriptional mechanisms in osteoblast differentiation and bone formation," *Trends in Genetics* **19**(8), 458–466 (2003).
8. N. K. Kaneshiro, "Large fontanelles," Available online: <https://medlineplus.gov/ency/imagepages/9335.htm>
9. R. Llorens-Salvador and A. Moreno-Flores, "The ABCs of transfontanelar ultrasound and more," *Radiologia* **58**, 129–141 (2016).
10. A. Tsai, R. Lasky, S. John, P. Evans, and K. Kennedy, "Predictors of neurodevelopmental outcomes in preterm infants with intraparenchymal hemorrhage," *J. Perinatol.* **34**(5), 399–404 (2014).
11. B. Y. Huang and M. Castillo, "Hypoxic-ischemic brain injury: imaging findings from birth to adulthood," *Radiographics* **28**(2), 417–439 (2008).
12. S. C. Carson, B. S. Hertzberg, J. D. Bowie, and P. C. Burger, "Value of sonography in the diagnosis of intracranial hemorrhage and periventricular leukomalacia: a postmortem study of 35 cases," *Am. J. Neuroradiol.* **11**(4), 677–683 (1990).
13. J. Intrapromkul, F. Northington, T. A. Huisman, I. Izbudak, A. Meoded, and A. Tekes, "Accuracy of head ultrasound for the detection of intracranial hemorrhage in preterm neonates: comparison with brain MRI and susceptibility-weighted imaging," *J. Neuroradiol.* **40**(2), 81–88 (2013).
14. L. V. Wang, "Tutorial on photoacoustic microscopy and computed tomography," *IEEE J. Sel. Top. Quantum Electron.* **14**(1), 171–179 (2008).
15. L. V. Wang and S. Hu, "Photoacoustic tomography: in vivo imaging from organelles to organs," *Science* **335**(6075), 1458–1462 (2012).
16. J. Xia, J. Yao, and L. V. Wang, "Photoacoustic tomography: principles and advances," *Electromagn. Waves (Camb.)* **147**, 1–22 (2014).
17. J. Yao and L. V. Wang, "Photoacoustic microscopy," *Laser Photonics Rev.* **7**(5), 758–778 (2013).
18. Y. Zhou, J. Yao, and L. V. Wang, "Tutorial on photoacoustic tomography," *J. Biomed. Opt.* **21**(6), 061007 (2016).
19. R. Manwar, M. Hosseinzadeh, A. Hariri, K. Kratkiewicz, S. Noei, and N. M. Avanaki, "Photoacoustic signal enhancement: towards utilization of low energy laser diodes in real-time photoacoustic imaging," *Sensors* **18**(10), 3498 (2018).
20. M. Zafar, K. Kratkiewicz, R. Manwar, and M. Avanaki, "Development of low-cost fast photoacoustic computed tomography: system characterization and phantom study," *Appl. Sci.* **9**(3), 374 (2019).
21. A. Fatima, K. Kratkiewicz, R. Manwar, M. Zafar, R. Zhang, B. Huang, N. Dadashzadesh, J. Xia, and M. Avanaki, "Review of cost reduction methods in photoacoustic computed tomography," *Photoacoustics* **15**, 100137 (2019).
22. L. V. Wang, *Photoacoustic Imaging and Spectroscopy* (CRC Press, 2009).
23. L. V. Wang and J. Yao, "A practical guide to photoacoustic tomography in the life sciences," *Nat. Methods* **13**(8), 627–638 (2016).
24. K. Kratkiewicz, R. Manwar, A. Rajabi-Estarabadi, J. Fakhoury, J. Meiliute, S. Daveluy, D. Mehregan, and K. M. Avanaki, "Photoacoustic/ultrasound/optical coherence tomography evaluation of melanoma lesion and healthy skin in a swine model," *Sensors* **19**(12), 2815 (2019).

25. K. Kratkiewicz, R. Manwar, M. Zafar, R. Zhang, B. Huang, N. Dadashzadesh, J. Xia, and M. Avnaki, "Review of cost reduction methods in photoacoustic computed tomography," In arXiv e-prints, 2019.
26. Rayyan Anwar, Karl Kratkiewicz, and Mohammed R. N. Avnaki, "Photoacoustic imaging: a promising alternative to transcranial ultrasound," Editorial Res. J. Photonics **2**, 1 (2018).
27. M. Zafar, K. Kratkiewicz, R. Manwar, and M. Avnaki, "Low-cost fast photoacoustic computed tomography: phantom study," In *Proceedings of Photons Plus Ultrasound: Imaging and Sensing* 2019; p. 108785V.
28. M. Mozaffarzadeh, A. Mahloojifar, M. Orooji, S. Adabi, and M. Nasirivanaki, "Double-stage delay multiply and sum beamforming algorithm: application to linear-array photoacoustic imaging," *IEEE Trans. Biomed. Eng.* **65**(1), 31–42 (2018).
29. M. Mozaffarzadeh, A. Mahloojifar, M. Orooji, K. Kratkiewicz, S. Adabi, and M. Nasirivanaki, "Linear-array photoacoustic imaging using minimum variance-based delay multiply and sum adaptive beamforming algorithm," *J. Biomed. Opt.* **23**(2), 026002 (2018).
30. P. Omid, M. Zafar, M. Mozaffarzadeh, A. Hariri, X. Huang, M. Orooji, and M. Nasirivanaki, "A novel dictionary-based image reconstruction for photoacoustic computed tomography," *Appl. Sci.* **8**(9), 1570 (2018).
31. L. Mohammadi, H. Behnam, J. Tavakkoli, and M. Avnaki, "Skull's photoacoustic attenuation and dispersion modeling with deterministic ray-tracing: towards real-time aberration correction," *Sensors* **19**(2), 345 (2019).
32. B. Laviña, "Brain vascular imaging techniques," *Int. J. Mol. Sci.* **18**(1), 70 (2016).
33. M. Nasirivanaki, J. Xia, H. Wan, A. Q. Bauer, J. P. Culver, and L. V. Wang, "High-resolution photoacoustic tomography of resting-state functional connectivity in the mouse brain," *Proc. Natl. Acad. Sci.* **111**(1), 21–26 (2014).
34. A. C. W. Constanciel Colas, C. Mougnot, T. Looi, S. Pichardo, and J. M. Drake, "Acoustic characterization of a neonate skull using a clinical MR-guided high intensity focused ultrasound system for pediatric neurological disorder treatment planning," *J. Ther. Ultrasound* **3**, P14 2014.
35. A. G. Noguera, *Propagation of Ultrasound Through Freshly Excised Human Calvarium*, University of Nebraska-Lincoln, 2012.
36. J. Yao and L. V. Wang, "Photoacoustic brain imaging: from microscopic to macroscopic scales," *Neurophotonics* **1**(1), 011003 (2014).
37. N. Meimani, N. Abani, J. Gelovani, and M. R. Avnaki, "A numerical analysis of a semi-dry coupling configuration in photoacoustic computed tomography for infant brain imaging," *Photoacoustics* **7**, 27–35 (2017).
38. R. Manwar, K. Kratkiewicz, and K. Avnaki, "Overview of ultrasound detection technologies for photoacoustic imaging," *Micromachines* **11**(7), 692 (2020).
39. B. D. Lindsey, E. D. Light, H. A. Nicoletto, E. R. Bennett, D. T. Laskowitz, and S. W. Smith, "The ultrasound brain helmet: New transducers and volume registration for in vivo simultaneous multi-transducer 3-D transcranial imaging," *IEEE Trans. Ultrason., Ferroelect., Freq. Contr.* **58**(6), 1189–1202 (2011).
40. B. Ihnatsenka and A. P. Boezaart, "Ultrasound: Basic understanding and learning the language," *Int. J. Shoulder Surg.* **4**(3), 55 (2010).
41. S. D. Vik, H. Torp, T. Follestad, R. Støen, and S. A. Nyrnes, "NeoDoppler: new ultrasound technology for continuous cerebral circulation monitoring in neonates," *Pediatr. Res.* **87**(1), 95–103 (2020).
42. S. Basiri-Esfahani, A. Armin, S. Forstner, and W. P. Bowen, "Precision ultrasound sensing on a chip," *Nat. Commun.* **10**(1), 132–139 (2019).
43. B. A. Angelsen, H. Torp, S. Holm, K. Kristoffersen, and T. Whittingham, "Which transducer array is best?" *European J. Ultrasound* **2**(2), 151–164 (1995).
44. W. Lee and Y. Roh, "Ultrasonic transducers for medical diagnostic imaging," *Biomed. Eng. Lett.* **7**(2), 91–97 (2017).
45. T. L. Szabo and P. A. Lewin, "Ultrasound transducer selection in clinical imaging practice," *J. Ultrasound in Med.* **32**(4), 573–582 (2013).
46. W. C. Vogt, C. Jia, K. A. Wear, B. S. Garra, and T. J. Pfefer, "Phantom-based image quality test methods for photoacoustic imaging systems," *J. Biomed. Opt.* **22**(9), 095002 (2017).
47. G. M. Ecury-Goossen, F. A. Camfferman, L. M. Leijser, P. Govaert, and J. Dudink, "State of the art cranial ultrasound imaging in neonates," *J. Vis. Exp.* **96**, e52238 (2015).
48. S. Na, J. J. Russin, L. Lin, X. Yuan, P. Hu, K. B. Jann, L. Yan, K. Maslov, J. Shi, and D. J. Wang, "Massively parallel functional photoacoustic computed tomography of the human brain," *Nat. Biomed. Eng.* **2021**, 1–9 (2021).
49. K. Kratkiewicz, R. Manwar, Y. Zhou, M. Mozaffarzadeh, and K. Avnaki, "Technical considerations in the Verasonics research ultrasound platform for developing a photoacoustic imaging system," *Biomed. Opt. Express* **12**(2), 1050–1084 (2021).
50. R. O. Bude and R. S. Adler, "An easily made, low-cost, tissue-like ultrasound phantom material," *J. Clin. Ultrasound* **23**, 271 (1995).
51. S. E. Bohndiek, S. Bodapati, D. Van De Sompel, S.-R. Kothapalli, and S. S. Gambhir, "Development and application of stable phantoms for the evaluation of photoacoustic imaging instruments," *PLoS One* **8**(9), e75533 (2013).
52. J. R. Cook, R. R. Bouchard, and S. Y. Emelianov, "Tissue-mimicking phantoms for photoacoustic and ultrasonic imaging," *Biomed. Opt. Express* **2**(11), 3193–3206 (2011).
53. W. C. Vogt, C. Jia, K. A. Wear, B. S. Garra, and T. J. Pfefer, "Biologically relevant photoacoustic imaging phantoms with tunable optical and acoustic properties," *J. Biomed. Opt.* **21**(10), 101405 (2016).
54. Z. Lu, J. He, Y. Yu, Z. Li, Z. Li, and J. Gong, "Measurement of lateral ventricle volume of normal infant based on magnetic resonance imaging," *Chin. Neurosurg. J.* **5**(1), 1–6 (2019).

55. T. F. Saxon, J. Colombo, E. L. Robinson, and J. E. Frick, "Dyadic interaction profiles in infancy and preschool intelligence," *J. School Psychol.* **38**(1), 9–25 (2000).
56. S.-V. Bodea and G. G. Westmeyer, "Photoacoustic neuroimaging-perspectives on a maturing imaging technique and its applications in neuroscience," *Front. Neurosci.* **15**, 655247 (2021).